Collective bacterial condensation is fundamentally constrained by the emergence of active turbulence.

Nir Livne and Ady Vaknin*

The Racah Institute of Physics, The Hebrew University, Jerusalem 91904, Israel

Running title: active turbulence constrains bacterial condensation.

*Corresponding author:

Mailing address:	The Racah Institute of Physics, The Hebrew University, Edmond J. Safra campus Jerusalem 91904, Israel
Phone:	(972) 658-4266
FAX:	(972) 658-6168
E-mail:	*avaknin@mail.huji.ac.il*

Keywords: bacterial chemotaxis | collective condensation | correlated swimming | active turbulence

Collective bacterial condensation arises from positive feedback between the ability of bacteria to generate chemical gradients and their chemotactic ability to track those gradients, resulting in the spontaneous formation of local cell accumulations. Here, by following the bacterial condensation dynamics in uniform acidic environments, we show that condensation is critically constrained by the spontaneous emergence of correlated bacterial swimming. Under the unique conditions prevailing within the condensate—characterized by sharp cell-density gradients and the absence of physical boundaries—correlated bacterial motion leads to vortex-like cell motion with an additional pronounced radial component directed down the cell-density gradient. This correlated motion induces active turbulence behavior associated with local fluid motion that broadens the condensate and expels non-chemotactic bacteria. However, when cells are embedded in a porous environment, correlated motion is suppressed, allowing spontaneous condensation to proceed further and form exceptionally dense bacterial accumulations. Overall, these findings highlight the fundamental interplay between self-generated bacterial condensation and correlated swimming.

Significance statement

Self-induced condensation and active turbulence are two prominent forms of collective bacterial behaviors. However, their interplay has not been experimentally studied. Here, we show that collective bacterial condensation gives rise to correlated swimming, which in turn fundamentally limits further condensation. Furthermore, we demonstrate that in dilute porous environments—common in natural bacterial habitats—correlated swimming is strongly suppressed, enabling the spontaneous formation of extremely dense cell condensates. These condensates may serve as a basis for the development of more structured bacterial communities.

Introduction

Motile bacteria navigate their environment by tracking chemical gradients toward regions they deem favorable (1-4). This behavior, termed chemotaxis, influences many aspects of bacterial ecology (5, 6) and human health (7-9). Even in spatially uniform environments, bacteria can collectively follow self-generated gradients, allowing them to accelerate their expansion into resource-rich regions (10, 11), or, alternatively, condense into focal points by either secreting beneficial (attractant) effectors (12, 13) or neutralizing harmful (repellent) effectors (14). Notably, in contrast to the inherently dynamic bacterial distributions triggered by exogenous chemoeffector release (15) or in expanding bacterial bands (16), bacterial condensation can lead to sharp but quasi-static bacterial accumulation (14). Condensation relies on positive feedback between self-generated gradients and the chemotactic responses of the bacteria to those gradients (Fig. 1A) that, in principle, can lead to a divergence in the local cell density (17). Studies of low cell-density and transient cell accumulations, limited by oxygen depletion, suggested that a fundamental limit on such cell condensation arises from the fact that chemotaxis itself is a non-local behavior (18). However, the constraints on bacterial condensations, under conditions of oxygen abundance, remain unclear. Here, we show that under these conditions, bacterial condensation is, in fact, limited by the emergence of correlated bacterial swimming and active turbulence.

Escherichia coli (E. coli) cells use rotating helical filaments (flagella) that bundle at the back of the cell and propel it forward. However, during stochastic episodes of counter-rotation the bundle comes apart, causing random reorientation of the cell. These two swimming modes—forward swimming (‘run’) and random reorientation (‘tumble’)—together generate an active random walk (19) with a typical run length (~10–30 μm). In the presence of effector gradients, the probability of tumbling is modulated to bias the random walk toward beneficial effectors and away from harmful ones. In particular, bacteria can migrate towards neutral pH (20, 21), which along with their ability to neutralize the environment, can lead to their

74 spontaneous, self-induced, condensation (14). Notably, this behavior is readily observed only
75 under conditions that the bacterial suspension is coupled to a large and cell-free environment
76 that keeps the pH level within the dynamic range of the sensory detection and prevents oxygen
77 depletion.

78 On the other hand, at high cell density, bacteria tend to exhibit correlated swimming and
79 flocking-like behavior (22-24), which can lead to turbulent-like motion often termed 'active
80 turbulence' (25, 26). However, the interplay between bacterial condensation and correlated
81 swimming was scarcely studied and remains unclear. Bacterial correlated swimming arises from
82 direct steric interactions and hydrodynamic interactions between cells. With notable exceptions
83 (27, 28), this behavior has mostly been studied in uniformly distributed populations confined by
84 physical boundaries. In contrast, bacterial condensation leads to highly non-uniform cell
85 distributions in the absence of explicit physical boundaries. Numerical studies have suggested
86 that dilute self-attracting run-and-tumble particles with rather weak chemotactic strength
87 aggregate less efficiently when self-induced fluid motion is considered (29). In addition,
88 experiments have suggested that cell alignment may constrain the angular rotation of individual
89 cells and thus reduce their chemotactic efficiency in uniform cell suspensions and shallow
90 effector gradients (30). However, other studies have shown that the tendency of cells to align
91 may, in fact, enhance their taxis efficiency toward a local source (31). Thus, how correlated
92 bacterial swimming may influence their collective condensation remains unclear.

93 Here, we investigate the limits of bacterial condensation under conditions where oxygen
94 deprivation and effector-saturation are not limiting factors. As a model, we used the recently
95 described assay for bacterial condensation in uniform acidic environments (14). We show that
96 stable bacterial condensation is sharply constrained by the emergence of correlated bacterial
97 swimming during cell accumulation. This correlated swimming gives rise to substantial
98 turbulent-like fluid motion, with averaged velocity characterized by vortex-like motion and with an
99 additional velocity component in the outward direction aligned with the downward cell-density

gradient. This fluid motion effectively exerts outward physical forces on the cells that counter the inward chemotaxis force. Interestingly, at very high cell densities the condensate becomes ring-shaped; yet, the radial component of the collective swimming was still aligned with the cell-density gradient. However, the characteristic vorticity in these condensates reverted between the outer and inner regions of the ring. Finally, we show that in porous environments, bacterial correlated motion is diminished without significantly affecting the chemotactic performance of cells. Consequently, bacterial condensation is considerably enhanced in porous media, approaching the low cell-density limit but with significantly higher cell densities.

Results

Bacterial condensation is constrained by the emergence of correlated swimming. To test the constraints on bacterial condensation in a controlled environment, we used the setup illustrated in Fig. 1B (see ref. 14). In this setup, free-swimming cells are confined within a shallow liquid layer (typically 120 μm thick), sandwiched between a glass slide and a larger hydrogel layer, which together form a uniformly low-pH environment (pH 5.2). Under these conditions, bacteria tend to collectively condense due to inherent feedback between the ability of the bacteria to neutralize their local pH and their chemotactic ability to swim towards neutral pH (14). While cells cannot penetrate the dense hydrogel mesh (3 % agarose), protons and oxygen readily diffuse across the thin bacterial layer and into the gel, preventing their rapid depletion inside the bacterial condensate and thereby enabling quasi-stable, high-density cell condensation (Fig. 1B, right plot).

By following the peak cell-density (ρ_{max}) and the width at half-maximum (*W*) of the cell distribution we identified two distinct temporal phases of the condensation (Fig. 1C). Initially, in phase 1, the peak cell-density ρ_{max} increased while the width *W* decreased, reflecting strong bacterial condensation. Then, beyond a critical time point (t_{sat}), in phase 2, the width *W* abruptly plateaued while ρ_{max} continued to rise, reflecting continued cell accumulation without further

125 narrowing of the condensate. These trends are further demonstrated in Fig. 1D, where the width
126 of the condensation is plotted against the maximum cell density for several repetitions. Notably,
127 the saturation value of the condensate width was substantially larger than the low-cell-density
128 limit previously reported in ref. 18. The spatial profile of the bacterial accumulation also reflected
129 this dynamical transition (Fig. 1D, inset). By normalizing each profile by ρ_{max} and the width by
130 *W*, the profiles collapsed onto a single curve in each phase, but these cumulative curves were
131 distinct between the two phases.

132 The dynamic transition described in Fig. 1D, was clearly associated with the appearance
133 of significant density fluctuations within the condensate (Fig. 1E). Initially (phase 1), the
134 bacterial condensate was smooth and stable (Fig. S1). However, beyond the critical time point
135 t_{sat}, pronounced spatial non-uniformity developed, with dynamic cell-density fluctuations on a
136 scale of approximately 20-100 μm (Fig. 1E, see also Supplementary Movie 1). These
137 fluctuations indicate correlated swimming of large groups of cells. Analysis of these dynamic cell
138 density fluctuations using particle image velocimetry (PIV; see Materials and Methods) revealed
139 that, on-average (~ 30 sec), cell motion is characterized by a vortex-like clockwise rotation of the
140 entire condensate with an additional radial component (Fig. 1E). Interestingly, the emergence of
141 the cell-density fluctuations and correlated swimming coincided with the dynamic transition at
142 t_{sat} (Fig. 1E).

143 **Fluid motion associated with the bacterial correlated swimming**. To characterize the fluid-
144 motion caused by the bacterial correlated swimming, we mixed passive green fluorescent beads
145 (1 μm in diameter) within the bacterial population, which in this case expressed red fluorescent
146 proteins (Fig. 2), and analyzed their motion by particle tracking (Materials and Methods).
147 Typically, the beads' trajectories included periods of local motion interrupted by approximately
148 directional movements, termed 'jets' (Fig. 2A). To elucidate the effect of the bacterial motion on
149 the beads, we evaluated for each jet the ratio $Pe = \upsilon \cdot L/D_{beads}$ (Péclet number), where υ and L are
150 the characteristic velocity and length of the jet, respectively, and D_{beads} is the diffusion constant

151 of the beads. This *Pe* characterizes the time required for a bead to traverse a typical distance
152 by fluid flow compared to the typical diffusion time associated with the same distance. The
153 cumulative distribution of *Pe* is shown in Fig. 2A (right plot) for trajectories within (green) or
154 outside (blue) the condensate region. Clearly, the beads' motion was substantially expedited
155 within the condensate.

156 Turbulent-like fluid motion can potentially also modulate the effector (H^+) distribution. To
157 evaluate the potential significance of this effect, we evaluated the *Pe* parameter for the protons
158 ($D_{protons} \sim 10^3 \cdot D_{beads}$), assuming protons follow the local fluid motion. Fig. 2B presents the
159 cumulative number of jets per bead, integrated over the diffusion time of protons across the
160 condensate $t_D = W^2/4D_{H+}$, where W is the width of the condensate. These data show that, on
161 average, each bead in the condensate experiences at least one substantial jet with $Pe > 0.5$
162 over the time t_D. We therefore conclude that, while cell-induced fluid motion can influence the
163 effector distribution, it is most likely not dominant.

164 As with the bacterial collective motion, averaging the beads' motion in time (90 sec)
165 reveals a vortex like fluid flow in the condensate (Fig. 2C–D). The spatial distributions of the
166 velocity components are shown in Fig. 2C, and the corresponding profile of the angular velocity
167 is shown in Fig. 2D, revealing a coordinated vortex like motion. Notably, in addition to the
168 tangential velocity contributing to vorticity, the flow field exhibited a substantial outward radial
169 component peaking at ~ 0.85 $\mu m \cdot s^{-1}$ near its half-width and extended throughout the
170 condensate. This outward radial velocity is comparable to *E. coli's* chemotactic drift velocity (19,
171 30). Additionally, we noted that above the condensed cells, which tended to occupy the lower-
172 half region of the fluid layer (~ 60 μm), the tracer beads exhibit an inward flow (Fig. 2E;
173 Supplementary Movie 2). Thus, the fluid motion in the vicinity of the condensate seem to exhibit
174 a three-dimensional toroidal pattern (Fig. 2F).

175 **Correlated swimming leads to expulsion of non-chemotactic cells**. Given the observed
176 fluid motion, and particularly the outward radial component, we tested its effect on the cells
177 within the condensate. We repeated the condensation experiments using a mixture of
178 chemotactic (wild-type, red-labeled) and low density non-chemotactic, smooth-swimming cells
179 (green-labeled). Because non-chemotactic cells are not subjected to the inward chemotactic
180 force, we expected them to be more sensitive to influence by the fluid motion. We found that as
181 the wild-type cells condensed, the non-chemotactic cells were expelled from the condensate
182 (Fig. 3). Additional run-and-tumble but non-chemotactic strain was tested (32), also showing
183 significant depletion, see Fig. S2 and related text. We expect this outward force to act also on
184 chemotactic cells; however, in their case, this force is balanced by an inward chemotactic force
185 that drives condensation. Still, such an outward force may influence the width of the
186 condensate.

187 **Porous environment suppresses correlated swimming and enhances condensation**.
188 Porous media is expected to dampen fluid flows due to the added drag with the porous scaffold
189 (33) and potentially inhibit correlations between bacteria. For example, porous media have been
190 suggested to inhibit bioconvection (34). Thus, to further test the effect of correlated swimming
191 on bacterial condensation, we conducted experiments in which cells were immersed in a thin
192 porous environment formed by a dilute agarose hydrogel instead of liquid (Fig. 4A). The rest of
193 the setup was unchanged. Using the channel chemotaxis assay described in ref. 21, we verified
194 that the bacterial chemotaxis performance in this porous environment was comparable to that in
195 liquid (Fig. S3). Moreover, by introducing opposing chemoeffectors at one end of the channel,
196 we triggered low cell-density accumulation. The agarose hydrogel had no detectable effect on
197 the cell-diffusion-driven broadening of this accumulation (Fig. S3).

198 In contrast, the porous environment had a dramatic effect on bacterial condensation and
199 correlated swimming (Fig. 4). Although the condensation proceeded at a rate similar to that in
200 liquid, in hydrogel it saturated only when the width of the condensate approached the low-

201 density limit of ~180 μm (18) (Fig. 4A-B). Correspondingly the cell density in these tightly
202 condensed bacterial populations became extremely high. As in liquid, in the porous
203 environment the shape of the bacterial condensate was modified when it reached its limit
204 (Fig. S4). Finally, the saturated condensates were also more compact in the vertical direction,
205 spanning only ~30 μm. Overall, in porous environments, the bacterial population spontaneously
206 condensed to its fundamental limit, reaching exceptionally high cell densities (Fig. S5), while the
207 cell population remained largely dynamic (Supplementary Video 3).

208 The enhanced condensation observed in porous environments was indeed associated
209 with a suppression of correlated swimming and associated fluid motion (Fig. S6 and Fig. 4C).
210 Furthermore, when we repeated the experiments with mixed populations of chemotactic and
211 non-chemotactic cells in the hydrogel environment, we found that, despite the strong
212 condensation of the chemotactic cells, the expulsion of the non-chemotactic cells was
213 significantly weaker (Fig. 4D). Taken together, these results further support the notion that
214 bacterial condensation in liquid is limited by the emergence of correlated swimming, rather than
215 merely the locally elevated density of the chemotactic cells.

216 **Ring-like condensation and the potential role of oxygen-taxis**. To test the condensation at
217 still higher cell densities, we repeated the experiments while increasing the initial (uniform) cell
218 density (Fig. 5). Since the well diameters used here were chosen such that only one
219 condensate is formed (14), we expected the overall cell density in the condensate to increase
220 accordingly. Yet, we find that in both liquid and porous media, following the initial condensation,
221 once enough cells accumulate, the peak density ceases to increase while the condensate
222 broadens and turns into a stable ring (Fig. 5). A likely cause for such ring formation is the
223 development of oxygen gradients around the condensate that induce an outward chemotactic
224 force (aerotaxis) (35). Compared with the liquid medium, in the porous environment ring
225 formation occurred at much higher cell density but at significantly lower total number of cells
226 (Fig. 5A). This difference may result from the fact that turbulent swimming in liquid weakens the

227 net inward force and can be more easily be dominated by aerotaxis. Additionally, in liquid,
228 aeration of the condensate by bacteria-mediated convection may support the accumulation of
229 higher cell numbers prior to ring formation.

230 Interestingly, we found that in liquid, following ring formation, the vorticity reverses
231 between the inner and outer regions of the 'aerotaxis' ring (Fig. 5C), including both the radial
232 and tangential components. We note, however, that the reversal of both components is
233 consistent with them being determined relative to the cell density gradient: in both cases the
234 collective motion flows radially down the cell density gradient and tends to exhibit also a
235 rightward lateral deflection (illustrated in Fig. 5C).

236 **Simplified model for condensate broadening**. To test whether the observed cell-induced fluid
237 motion (Fig. 2) can indeed lead to repulsion of non-chemotactic cells (Fig. 3) and broaden the
238 condensation of wild-type cells, we used Keller-Segel type chemotaxis model (36) that describes
239 the bacterial condensation in such acidic environment (14, 37):

240
$$\frac{\partial \rho}{\partial t} = \vec{\nabla} \cdot \left(D \vec{\nabla} \rho - \rho \vec{v}_D \right) \qquad (1)$$
$$\frac{\partial c}{\partial t} = D_c \nabla^2 c - r_H \rho c \qquad (2)$$

241 Here, D is the active diffusion of the cells, v_D is their drift velocity, D_c is the effective proton
242 diffusion coefficient, and r_H is the proton-removal rate. Note that bacteria are not growing in
243 these experiments. Following ref. 38, the chemotaxis-induced drift velocity was modeled as
244 $\vec{v}_D = \beta \vec{\nabla} \ln\left(c + K_{off}/c + K_{on}\right)$ where K_{on} and K_{off} are the effective dissociation constants for the
245 chemoreceptors in the ON or OFF states, and β is the chemotaxis coefficient. The proton-
246 removal rate was given the empirical form $r_H = \gamma c^{1/2}$ (14). The cell density dynamics was
247 assumed to be two dimensional and radially-symmetric, occupying the top layer of a three-
248 dimensional proton field. For more details see Supplementary Information. This model
249 accurately describes the shape of condensates in phase 1 (Fig. 6A). However, it predicts much

250 sharper condensation and a different shape than those observed experimentally in phase 2
251 (Fig. 6B, dashed blue line).

252 Thus, considering the random fluid motion at short time scales with the added outward
253 averaged drift component observed in Fig. 2, we suggest that bacteria subjected to such fluid
254 motion experience not only the inward chemotactic force, but also an additional outward drift.
255 Since this radial velocity was found to be proportional to the cell-density gradient (Figs. 2C, 5C,
256 and S7), we added a drift velocity of the form:

257 $$\vec{U} = -\eta \cdot \vec{\nabla}(\rho/\rho_0) \qquad (3)$$

258 with $\eta = 10^{-7}$ cm^2s^{-1} and ρ_0 the initial (uniform) cell density ($\rho_0 \sim 0.7 \cdot 10^6$ cells·mm^2). Indeed,
259 adding this fluid-induced velocity component to the model can strictly limit the condensation and
260 account for the broadening and shape of mature condensates during phase 2 (Fig. 6A-B, black
261 lines). Notably, adding the drift velocity from the beginning of the simulation resulted in a
262 gradual transition between phase 1 and phase 2, which does not agree with the sharp transition
263 observed in the experiments (Figs. 1C and 6B). However, adding this velocity only above a
264 certain threshold cell density clearly accounts for the observed transition (Fig. 6B). This is
265 consistent with the emergence of the correlated motion only above a certain cell density (Fig. 1).
266 The added drift velocity can also account for the expulsion of non-chemotactic cells from the
267 condensate (Fig. 6C, see also Fig. 3 and Supplementary Information).

268 Finally, we also considered the potential influence of correlated swimming on the
269 chemotaxis efficiency (30, 39). First, we note that for such influence to limit condensation, it
270 must reduce the chemotaxis efficiency. To incorporate this into the model, we allowed the
271 chemotactic coefficient (β) to depend on the local cell-density according to the findings in ref. 30
272 (Fig. S8). Clearly, such an effect can also contribute to limiting the condensation (Fig. 5B,
273 orange line). However, modulating the chemotaxis efficiency cannot lead to repulsion of non-
274 chemotactic cells.

275 The overall relationship between the initial cell density and condensation is summarized
276 in Fig. 6D. When the initial cell density is below approximately $0.4 \cdot 10^6$ cells/mm^2, no
277 condensation is observed (14, 37). At higher densities, the initially uniform distribution becomes
278 unstable, and condensation emerges. In the absence of corelated swimming, the bacteria can
279 condense until the local cell density becomes sufficient to raise the local pH beyond the sensory
280 dynamic range of the cells (blue line, see also ref. 14). However, because correlated swimming
281 readily emerges, bacterial condensation is severely restricted (simulations: dark-gray line; data:
282 red circles). In contrast, in porous media, condensation proceeds further (gray circles), though
283 still limited below the value set by the dynamic range (blue line), likely due to the non-local
284 nature of bacterial gradient sensing (18). At even higher cell densities, condensation becomes
285 limited by ring formation, likely due to aerotaxis (Fig. 5).

286 **Discussion**

287 Chemotaxis-mediated condensation and correlated swimming are two prominent collective
288 behaviors exhibited by motile bacteria. Here, we describe a fundamental interplay between
289 these behaviors. We show that bacterial condensation is fundamentally constrained by the
290 emergence of correlated swimming (Figs. 1 and 6). In liquid, bacterial condensation proceeds in
291 two dynamic phases: initially, the bacterial population condenses and the local cell density
292 increases; then, upon the onset of correlated swimming, the width of the condensate plateaus
293 while cell density continues to rise. These bacterial condensates —characterized by steep cell-
294 density gradients and lack of physical boundaries— give rise to a distinct form of active
295 turbulence, with a radial component aligned down the cell-density gradient (Figs. 1 and 5).
296 Furthermore, we find that correlated swimming is suppressed in porous environments, enabling
297 exceptionally robust bacterial condensation with extremely high cell density (Fig. 4).

298 By imposing active turbulence, correlated swimming not only constrains bacterial
299 condensation but also expels non-chemotactic bacteria from the condensate, effectively leading

300 to segregation of the initially mixed population into chemotactic and non-chemotactic
301 subcommunities (Fig. 3). Previous experiments demonstrated bacterial expulsion from a local
302 vortex generated by rotating magnetic microspheres at 2–40 Hz (27). Here, however, the
303 condensates exhibit much weaker vorticity (~10^{-3} Hz). Moreover, the expulsion effect is
304 substantially reduced in a porous environment, where the local cell density in the condensate is
305 approximately 10-fold higher, but correlated swimming is absent (Fig. 4). Taken together, these
306 observations suggest that the expulsion of non-chemotactic cells is not merely due to the
307 imposed vorticity or the accumulation of the chemotactic cells. Instead, we suggest that this
308 expulsion is driven by the outward fluid flow generated by correlated swimming, which imposes
309 an outward velocity bias (Eq. 3 and Fig. 6). Notably, this radial velocity bias, generically aligns
310 with the bacterial density gradient, even in ring-shaped condensates (Figs. 1,2, 5 and S7),
311 consistent with the observation that correlated swimming is enhanced at high cell densities (28)
312 but fades as cells move down the density gradient.

313 Correlated bacterial swimming and active turbulence can influence condensation through
314 two additional mechanisms. First, by promoting advection of chemotactic effectors (in this case,
315 protons), which can limit the buildup of steep gradients. We find that over a time period
316 corresponding to the diffusion time across the condensate, each probe particle typically
317 experiences at least one significant event that enhances its motion beyond simple diffusion, i.e.,
318 with $Pe > 0.5$ (Fig. 2B). This suggests that while advection may not dominate over diffusion, it
319 can be significant. Second, correlated swimming may directly affect chemotaxis efficiency by
320 altering run-and-tumble dynamics. This effect, however, been shown to enhance bacterial
321 accumulation near local attractive sources (31) but has also been shown to either improve or
322 impair chemotaxis efficiency in shallow gradients, depending on cell density (30). Although this
323 effect could potentially contribute to the observed broadening of the condensation (Fig. 6), it
324 remains unclear to what extent such modulation of chemotaxis efficacy is effective under sharp

325 gradients of both the effector distribution and cell-density. In any case, these effects cannot
326 account for the observed expulsion of non-chemotactic cells.

327 Bacterial suspensions confined in small cylindrical wells (~ 45 μm diameter) have been
328 shown to exhibit vortex-like motion with a random direction, whereas in larger wells, chaotic
329 motion develops without coherent vorticity (40). In contrast, the correlated swimming observed
330 here is consistently characterized by clockwise vorticity of the entire condensate, (~ 600 μm
331 diameter), as viewed from the glass side (Figs. 1–2). At higher cell densities, when the
332 condensate develops a ring-like structure the vorticity reverses between the inner and outer
333 regions of the ring (Fig. 5C). Because the radial velocity also reverses across the ring, a global
334 rightward swimming tendency is maintained (Fig. 5C), consistent with the circular motion
335 observed when non-interacting individual cells swim near glass surfaces (< 1 μM; Fig. S9) (41).
336 However, bacterial condensates extend up to 60 μm from the surface and are far denser. We
337 suggest that interactions with the nearby surface, while unable to generate strong vorticity on
338 their own, may nevertheless break the symmetry and promote clockwise bias to otherwise
339 chaotic motion.

340 The distinct swimming behaviors observed here may also be related to the unique
341 properties of the bacterial condensate. In general, but with notable exceptions (28, 42), active
342 turbulence has been studied in uniform cell populations confined by well-defined lateral
343 boundaries, either solid (43) or at liquid–air or liquid–oil interfaces (43-46). In such settings, the
344 bacterial behavior near the lateral physical boundaries may play an important role in shaping the
345 observed swimming patterns (44, 47). In contrast, the bacterial condensate examined here
346 represents a unique system: a self-sustained yet highly non-uniform cell suspension lacking
347 lateral physical boundaries. The fluid motion in the vicinity of the condensate exhibits a three-
348 dimensional toroidal pattern (Fig. 2F), reminiscent of the flow patterns observed in bioconvection
349 (34, 48). However, in bioconvection it arises due to instability caused by upward bacterial taxis
350 opposing the downward gravitational force. More complex behavior has been observed when

351 metallic particles were also driven up and down by the applied voltage of the sample (49). In
352 contrast, the bacterial condensate is overall stable, and the fluid motion arises directly from local
353 bacterial motion combined with the strong cell density gradients imposed by the inward
354 chemotaxis force.

355 Correlated bacterial swimming was clearly suppressed in porous environments, leading
356 to exceptionally dense cell condensates (Fig. 4). Notably, experiments conducted in mucin-
357 containing media at neutral pH still exhibit correlated swimming, albeit with larger vortex size
358 (50). Interestingly, however, the agarose-based hydrogel used here more closely resembles
359 mucin-containing media at low pH (51), which may be more relevant to certain physiological
360 conditions than neutral pH. Moreover, the enhanced condensation observed under these
361 conditions may facilitate the formation of more structured biofilm communities.

362 Materials and Methods

363 **Strains and plasmids.** We used *E. coli* MG1655 (VF6 (32, 52)) and its derivatives harboring
364 deletion of *cheY* and *cheZ* (MK3) or deletions of all chemoreceptors and a dysfunctional *cheZ*
365 gene (non-chemotactic run-and-tumble cells (AVE4 (32)). Cells expressed also a fluorescent
366 mGFP (75 μM IPTG) or mCherry (5 mM) from a pTrc99a vector (pSA11).

367 **Cell growth and motility medium.** Cells were grown over night in Tryptone Broth (TB, tryptone
368 extract 10 g/l and 5 g/l NaCl) supplemented with Ampicillin, diluted 100-fold into fresh medium
369 with IPTG, and allowed to grow at 33.5 °C with shaking. Cells were harvested at an OD_{600} of 0.5
370 by centrifugation and gently washed twice in motility medium and resuspended in motility
371 medium with final cell concentration of OD_{600} 0.4 (unless otherwise mentioned). The motility
372 medium (0.1 mM potassium phosphate, 0.94 mM lactic acid, 85.5 mM sodium chloride, 0.1 mM
373 EDTA, and 1 μM methionine) titrated to the desired pH with NaOH. Notably, this medium
374 supports long-term bacterial motility but not cell proliferation. Experiments in porous medium

375 (Fig. 4) were done gently mixing the cell suspension with agarose hydrogel at 37 °C to a final
376 agarose concentration of 0.08%.

377 **The condensation setup.** The setup used here is schematically illustrated in Fig. 1a. For more
378 details see ref. 14. An agarose gel (3% in motility medium) was casted in a cylindrical chamber
379 made from grade-2 titanium (6 mm height, 10.7mm diameter) and sealed at the top with a mold
380 with a thin cylindrical protrusion (~120 μm high, and radius of ~ 3 or 5 mm), which will form the
381 bacterial layer; fabricated using a resin printer (Elegoo Mars 3). After the agarose solidified, the
382 mold and the bottom cover were removed and the agarose was dialyzed overnight in motility
383 buffer and a second time, for an additional 4 h, in a fresh motility buffer just before the
384 experiment (final dialysis ratio of 10^4:1). Bacterial cells were then introduced into the shallow
385 well, suspended in either liquid or soft agarose (0.08%), and the bottom and top of the chamber
386 were covered with BSA-treated glass coverslips (1% bovine serum albumin in double-distilled
387 water for 30 minutes) and secured in position. Experiments were performed at room
388 temperature (24 °C).

389 **Fluorescence microscopy.** The bacterial distribution was followed by using a Nikon Ti
390 microscope equipped with a 20× (0.5 NA) or 4× (0.2 NA) objective, a decoded controlled stage
391 and a 'perfect-focus' system. Large images were obtained by stitching smaller images
392 (approximately 2mm× 2mm each) with 20% overlap using a built-in function in NIS Elements
393 software (Nikon). The bacterial distribution inside the well was extracted from the images by
394 removing the measured background intensity and normalizing to the average intensity within
395 each well. Radial averaging was done by measuring the fluorescence intensity around the
396 center of focal points (Radial Profile Angle plugin for ImageJ).

397 **Cell density estimates.** Due to inhomogeneity of the cell distribution in the vertical direction
398 (see Fig. 2F), cell distributions are shown in cells/mm^2. Calibration of OD_{600} to cells/mm^3 was
399 done by plating serial dilution of cells after growth (OD_{600} 0.5), yielding OD_{600} 0.5 ≈ $7.2 \cdot 10^9$

400 cfu/mm^3. Surface density was then estimated by multiplying the cell density (ρ_{3D}), averaged
401 over the vertical direction (z), by the well height (h): $\rho = h\langle\rho_{3D}\rangle_z$.

402 **Non-uniformity estimates.** To determine the non-uniformity of the cell distribution within
403 condensates from still images, where temporal averaging is unavailable, a smooth radially-
404 averaged version of each image was subtracted from the original ones. A high-pass filter was
405 then applied to remove residual, large-scale intensity fluctuations (0-140 μm). Non-uniformity
406 was then measured as the difference between the standard deviation of the intensity within a
407 disk around the condensate center (600 μm diameter) and away from it.

408 **Fluorescent spheres.** In the experiments presented in Fig. 2, we used green fluorescent
409 spheres (beads) with a 1μm diameter (FluoSpheres, ThermoFisher Scientific). Before use,
410 spheres were thoroughly washed in motility medium to which Tween-20 (0.01%) was added.
411 The spheres were then added to a cell suspension, which also contained Tween-20 (0.01%).
412 The added Tween-20 prevented self-aggregation of the fluorescent spheres but had no
413 detectable effect on the bacterial condensation.

414 **Particle image velocimetry (PIV).** To capture velocity fields, time-lapse fluorescent images (2-
415 10 frames per second) were captured and analyzed by PIV using PIVLab (53). To analyze the
416 collective motion of cells, a filtering procedure was first applied to remove the large-scale
417 bacterial condensation (see Non-uniformity estimates) and a nearest-neighbors smoothing
418 scheme was applied to remove residual noise. PIV analysis proceeded using multipass FTT
419 window deformation (4 passes) with the final interrogation window being 16-18 pixels (64–
420 72 μm). To avoid false detection, only vectors with a correlation coefficient larger than 0.5 were
421 kept. The PIV parameters were chosen to balance between the resolution of the extracted
422 velocity field and the signal-to-noise ratio; changing them did not modify the results significantly.
423 To analyze the motion of the fluorescent beads, an initial mask was applied to ensure only
424 particles within the focal plane were analyzed. This was possible since beads within the focal

plane seem smaller and brighter than beads in other planes (see SI Video 3). Despite the BSA treatment, beads slowly adhered to the glass coverslip. By subtracting the median image from the time lapse, only non-adhered beads were analyzed. Analysis then proceeded in PIVLab as described for the bacteria.

Particle tracking and detection of jets. Time lapse images (2 frames per second) of the fluorescent beads were masked to ensure only particles within the focal plane are analyzed (see Particle image velocimetry (PIV)). Tracking was then performed using the TrackMate plugin for ImageJ. Detected tracks were exported and analyzed separately. Each track was smoothed using a Savgol-Golay filter (5 frames window) and velocities were estimated numerically. Jets were detected as temporal peaks in the velocity magnitude with a mean prominence of more than 0.5 μm/s. The length of each track (L) and it's mean velocity (v) were captured. If neighboring beads, less than L apart, exhibited a jet in the same direction ($\Delta\theta < 0.15$), their jets were considered as correlated; the velocity of such jets were averaged over and considered as one. Due to the low density of beads, such events were rare (7 of the 2362 detected jets).

Numerical solution of the model. Solutions and parameters were based on (14) and full details can be found in the Supp. Text. Briefly, the dynamics of cells was modeled in 2D assuming radial symmetry and the dynamics of protons was modeled in 3D assuming cylindrical symmetry. Proton uptake in the bacterial layer was accounted for by imposing absorbing boundary conditions for the protons at the bacterial layer interface. Numerical solutions were obtained by calculating spatial derivatives with 2nd order accuracy and using a 4th order Runge-Kutta method for time integration.

Author Contributions

NL and AV designed the experiments; NL performed the experiments and theoretical calculations; NL and AV analyzed the data and wrote the manuscript.

Acknowledgments

We thank Alexander Feigel (Hebrew University) and Igor Aronson (Penn. State University) for help full conversations. We thank the Milner Foundation for partly funding NL's fellowship. This work was supported by the Israeli Foundation of Sciences and Humanities and by a research grant from the U.S.-Israel Binational Science Foundation.

Competing Interest Statement: The authors declare no competing interests.

Data Availability Statement: All data is available upon request.

References

1. Berg HC (2004) *E. coli in Motion* (Springer, NY).
2. Parkinson JS, Hazelbauer GL, & Falke JJ (2015) Signaling and sensory adaptation in *Escherichia coli* chemoreceptors: 2015 update. *Trends Microbiol.* 23(5):257-266.
3. Colin R & Sourjik V (2017) Emergent properties of bacterial chemotaxis pathway. *Curr. Opin. Microbiol.* 39:24-33.
4. Moore JP, Kamino K, & Emonet T (2021) Non-genetic diversity in chemosensing and chemotactic behavior. *Int. J. Mol. Sci.* 22(13):6960.
5. Keegstra JM, Carrara F, & Stocker R (2022) The ecological roles of bacterial chemotaxis. *Nat. Rev. Microbiol.*
6. Raina J-B*, et al.* (2022) Chemotaxis shapes the microscale organization of the ocean's microbiome. *Nature* 605(7908):132-138.
7. Matilla MA & Krell T (2018) The effect of bacterial chemotaxis on host infection and pathogenicity. *FEMS Microbiol Rev* 42(1).
8. Butler SM & Camilli A (2005) Going against the grain: chemotaxis and infection in *Vibrio cholerae*. *Nat. Rev. Microbiol.* 3(8):611-620.
9. Zhou B, Szymanski CM, & Baylink A (2023) Bacterial chemotaxis in human diseases. *Trends Microbiol.* 31(5):453-467.
10. Cremer J*, et al.* (2019) Chemotaxis as a navigation strategy to boost range expansion. *Nature* 575(7784):658-663.
11. Adler J (1966) Chemotaxis in bacteria. *Science* 153:708-716.
12. Budrene EO & Berg HC (1991) Complex patterns formed by motile cells of *Escherichia coli*. *Nature* 349(6310):630-633.
13. Park S*, et al.* (2003) Motion to Form a Quorum. *Science* 301(5630):188-188.
14. Livne N, Koler M, & Vaknin A (2024) Collective condensation and auto-aggregation of *Escherichia coli* in uniform acidic environments. *Comm. Biol.* 7(1):1028.
15. Brumley DR*, et al.* (2019) Bacteria push the limits of chemotactic precision to navigate dynamic chemical gradients. *Proc. Natl. Acad. Sci.* 116(22):10792-10797.
16. Fu X*, et al.* (2018) Spatial self-organization resolves conflicts between individuality and collective migration. *Nat. Comm.* 9(1):2177.
17. Childress S & Percus JK (1981) Nonlinear aspects of chemotaxis. *Mathematical Biosciences* 56(3):217-237.
18. Mittal N, Budrene EO, Brenner MP, & Van Oudenaarden A (2003) Motility of *Escherichia coli* cells in clusters formed by chemotactic aggregation. *Proc. Natl. Acad. Sci.* 100(23):13259-13263.
19. Berg HC & Brown DA (1972) Chemotaxis in *Escherichia coli* analysed by three-dimensional tracking. *Nature* 239(5374):500-504.
20. Yang Y & Sourjik V (2012) Opposite responses by different chemoreceptors set a tunable preference point in Escherichia coli pH taxis. *Mol. Microbiol.* 86(6):1482-1489.
21. Livne N & Vaknin A (2022) Collective responses of bacteria to a local source of conflicting effectors. *Sci. Rep.* 12(1):4928.
22. Toner J & Tu Y (1998) Flocks, herds, and schools: A quantitative theory of flocking. *Phys. Rev. E* 58(4):4828-4858.

23. Wensink HH, *et al.* (2012) Meso-scale turbulence in living fluids. *Proc. Natl. Acad. Sci.* 109(36):14308-14313.
24. Koch DL & Subramanian G (2011) Collective hydrodynamics of swimming microorganisms: Living fluids. *Annl. Rev. Fluid Mechanics* 43(Volume 43, 2011):637-659.
25. Aranson IS (2022) Bacterial active matter. *Rep. Prog. Phys.* 85(7).
26. Alert R, Casademunt J, & Joanny J-F (2022) Active turbulence. *Annl. Rev. Cond. Matt. Phys.* 13(Volume 13, 2022):143-170.
27. Sokolov A & Aranson IS (2016) Rapid expulsion of microswimmers by a vortical flow. *Nat. Commun.* 7(1):11114.
28. Sokolov A, Aranson IS, Kessler JO, & Goldstein RE (2007) Concentration dependence of the collective dynamics of swimming bacteria. *Phys. Rev. Lett.* 98(15):158102.
29. Lushi E, Goldstein RE, & Shelley MJ (2012) Collective chemotactic dynamics in the presence of self-generated fluid flows. *Phys. Rev. E* 86(4):040902.
30. Colin R, Drescher K, & Sourjik V (2019) Chemotactic behaviour of *Escherichia coli* at high cell density. *Nat. Commun.* 10(1):5329.
31. Kai T, *et al.* (2024) Collective gradient sensing by dilute swimming bacteria without clustering. *Phys. Rev. Res.* 6(3):L032061.
32. Tamar E, Koler M, & Vaknin A (2016) The role of motility and chemotaxis in the bacterial colonization of protected surfaces. *Sci. Rep.* 6:19616.
33. Brinkman HC (1949) A calculation of the viscous force exerted by a flowing fluid on a dense swarm of particles. *Flow, Turbulence and Combustion* 1(1):27-34.
34. Bees MA (2020) Advances in bioconvection. *Annl. Rev. Fluid Mech.* 52(Volume 52, 2020):449-476.
35. Taylor BL, Zhulin IB, & Johnson MS (1999) Aerotaxis and other energy-sensing behavior in bacteria. *Annu. Rev. Microbiol.* 53:103-128.
36. Keller EF & Segel LA (1971) Traveling bands of chemotactic bacteria: a theoretical analysis. *J. Theor. Biol.* 30(2):235-248.
37. Livne N, Vaknin A, & Agam O (2025) Pattern formation in *E. coli* through negative chemotaxis: Instability, condensation, and merging. *Phys. Rev. Res.* 7(2):023095.
38. Si G, Wu T, Ouyang Q, & Tu Y (2012) Pathway-based mean-field model for *Escherichia coli* chemotaxis. *Phys. Rev. Lett.* 109(4):048101.
39. Miller M & Toner J (2024) Following your nose: Autochemotaxis and other mechanisms for spinodal decomposition in flocks. *Phys. Rev. Lett.* 132(12):128301.
40. Nishiguchi D, Shiratani S, Takeuchi KA, & Aranson IS (2025) Vortex reversal is a precursor of confined bacterial turbulence. *Proc. Natl. Acad. Sci. USA* 122(11):e2414446122.
41. Lauga E, DiLuzio WR, Whitesides GM, & Stone HA (2006) Swimming in circles: motion of bacteria near solid boundaries. *Biophys J* 90(2):400-412.
42. Sokolov A, Rubio LD, Brady JF, & Aranson IS (2018) Instability of expanding bacterial droplets. *Nat. Commun.* 9(1):1322.
43. Nishiguchi D, Aranson IS, Snezhko A, & Sokolov A (2018) Engineering bacterial vortex lattice via direct laser lithography. *Nat. Commun.* 9(1):4486.

44. Wioland H, Woodhouse FG, Dunkel J, Kessler JO, & Goldstein RE (2013) Confinement stabilizes a bacterial suspension into a spiral vortex. *Phys. Rev. Lett.* 110(26):268102.
45. Vincenti B*, et al.* (2019) Magnetotactic bacteria in a droplet self-assemble into a rotary motor. *Nat. Commun.* 10(1):5082.
46. Nishiguchi D, Shiratani S, Takeuchi KA, & Aranson IS (2025) Vortex reversal is a precursor of confined bacterial turbulence. *Proc Natl Acad Sci U S A* 122(11):e2414446122.
47. Lushi E, Wioland H, & Goldstein RE (2014) Fluid flows created by swimming bacteria drive self-organization in confined suspensions. *Proc. Natl. Acad. Sci. (USA)* 111(27):9733-9738.
48. Abe T, Nakamura S, & Kudo S (2017) Bioconvection induced by bacterial chemotaxis in a capillary assay. *Biochem. Biophys. Res. Comm.* 483(1):277-282.
49. Sapozhnikov MV, Tolmachev YV, Aranson IS, & Kwok WK (2003) Dynamic self-assembly and patterns in electrostatically driven granular media. *Phys. Rev. Let.* 90(11):114301.
50. Liao W & Aranson IS (2023) Viscoelasticity enhances collective motion of bacteria. *PNAS Nexus* 2(9).
51. Celli J*, et al.* (2005) Viscoelastic properties and dynamics of porcine gastric mucin. *Biomacromolecules* 6(3):1329-1333.
52. Frank V, Piñas GE, Cohen H, Parkinson JS, & Vaknin A (2016) Networked chemoreceptors benefit bacterial chemotaxis performance. *mBio* 7(6).
53. Thielicke W & Sonntag R (2021) Particle Image Velocimetry for MATLAB: Accuracy and enhanced algorithms in PIVlab. *J. Open Res. Soft.*

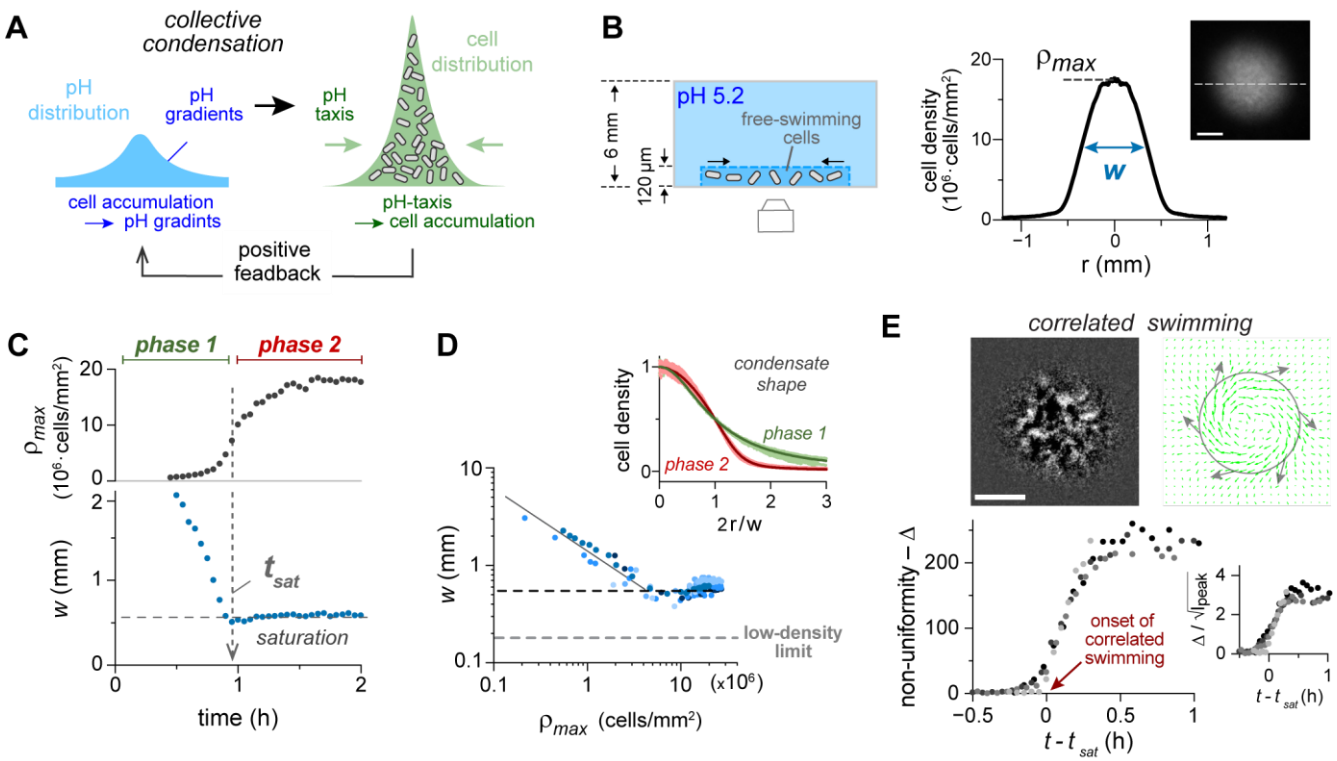

Figure 1. Bacterial condensation is constrained by correlated swimming. (A) Schematic of bacterial condensation in acidic environments (see ref. 14). Bacteria neutralize their vicinity and generate pH gradients in an otherwise uniform acid medium. At the same time, cells are chemotactically attracted toward neutral pH. These behaviors form reinforcing feedback that derives condensation. **(B)** The experimental setup consists of a thin GFP-expressing cell suspension (5 mm diameter) confined in a circular well made by 3% agarose gel. Both the cell suspension and the surrounding gel initially form a uniform acidic environment (pH 5.2). Condensation was monitored using fluorescence microscopy. Shown on the right is a typical mature condensate 2 h after initiation (scale bar: 300 µm), along with the radially averaged cell-density profile. The peak cell density (ρ_{max}) and the width at half maximum (w) are marked. **(C)** A typical condensation dynamic, characterized by increasing ρ_{max} and decreasing w until w abruptly saturates at time t_{sat}. **(D)** The condensate width (w) is plotted against peak cell density (ρ_{max}) for 7 independent experiments. The solid gray line reparents a power-law slope of -2/3. The saturation value of w (dark-gray dashed line) and the corresponding value measured at low cell density (light-gray dashed line, ref. 18) are indicated. *Inset* – normalized cell density profiles observed at different time points for 3 independent experiments: profiles taken at $t < t_{sat}$ (phase 1) are labeled green and profiles taken at $t > t_{sat}$ (phase 2) are labeled red. Each profile was normalized by subtracting the background intensity and dividing by the peak intensity; the radial coordinate was normalized by $w/2$. **(E)** *Upper-panel* – A typical filtered fluorescence image of the condensate (left, see Materials and Methods and SI Video 1; scale bar: 300 µm) and the corresponding time-averaged (30 s) velocity field obtained by particle image velocimetry (right, grey arrows are a guide to the eye). These are demonstrating the dynamic non-uniformity developed at high cell density. *Lower panel* – The non-uniformity within condensates (Δ), evaluated within the area r ≤ 300 µm, is plotted over time for 4 independent experiments (see Materials and Methods). *Inset* – The relative non-uniformity ($\Delta / \sqrt{I_{peak}}$) plotted over time.

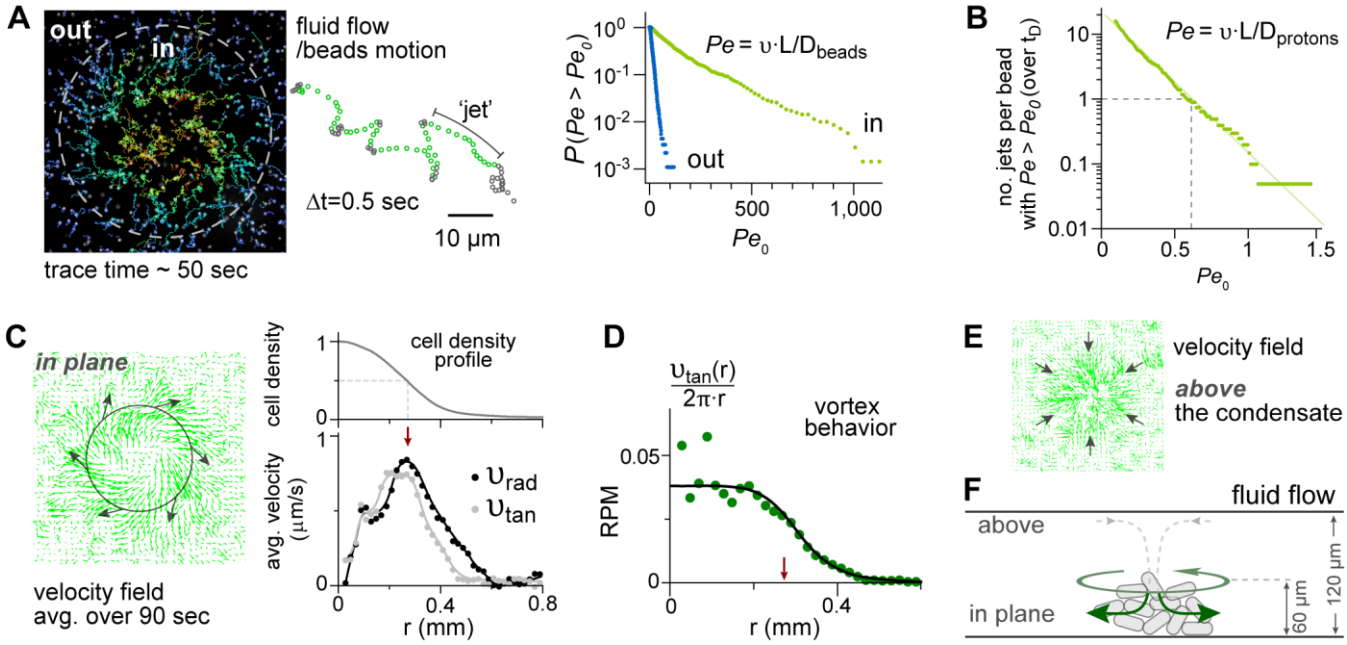

Figure 2. Fluid motion within the condensate. Fluid motion was assessed by tracking 1 μm beads (green fluorescent) mixed in the bacterial suspension. In this case, cells were labeled with mCherry (red). (**A**) Traces of individual beads (over 50 sec) within a mature condensate, using particle tracking analysis (Materials and Methods). The dashed white circle indicates the contour of the condensate width (w ~ 550 μm). A typical trace is highlighted on the right, illustrating intermittent motion composed of periods of local random motion (gray symbols) and periods of directed motion, termed 'jets' (green symbols). The length (L) and average speed (u) of each jet were used to calculate $Pe = u \cdot L/D_{beads}$ (with $D_{beads} = 5 \cdot 10^{-9}$ cm^2 s^{-1}). The cumulative distribution of Pe is shown on the right for beads inside or outside the area defined by the width of the condensate (dashed line). (**B**) Comparison of the beads motion (using 90 sec traces) with the expected proton diffusion. First, the number of jets per bead with a Pe value larger than a given threshold (Pe_0) were found and then multiplied by the typical diffusion time of protons across the condensate $t_D \sim w^2/4D_{H+} \sim 4$min (using $D_{H+} = 5 \cdot 10^{-6}$ cm^2 s^{-1}). (**C**) Time-averaged velocity field (averaged over 90 sec) in the condensate plane, extracted using PIV (Materials and Methods). Profiles of the radial and tangential velocity components are shown on the right alongside the corresponding (normalized) cell density profile. The red arrow marks the condensate width (w). (**D**) The angular velocity profile, revealing correlated vortex-like motion. Clockwise direction was chosen as positive. (**E**) Measured velocity field above the condensate (h ~ 100 μm) showing a radially-inward flow. (**F**) Schematic summarizing the inferred fluid motion in the vicinity of the condensate (see also Supplementary Video 2).

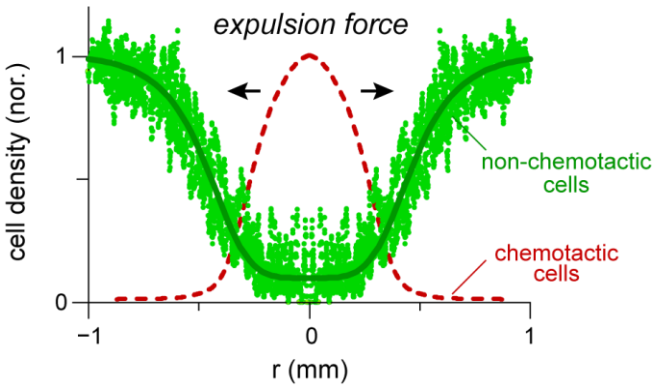

Figure 3. Non-chemotactic cells are forced out of the condensate. Chemotactic cells (mCherry labeled) and non-chemotactic cells (*ΔcheY/Z*; GFP labeled) were initially mixed in a 100:1 ratio, respectively, and applied to the setup shown in Fig. 1B. The cell-density profiles of the non-chemotactic cells in a mature condensate are shown (green symbols; 3 independent experiments), along with the corresponding profile of the condensate (red dashed line). Profiles were normalized to the background density and divided by a factor of 3000 (red) and 1 (green).

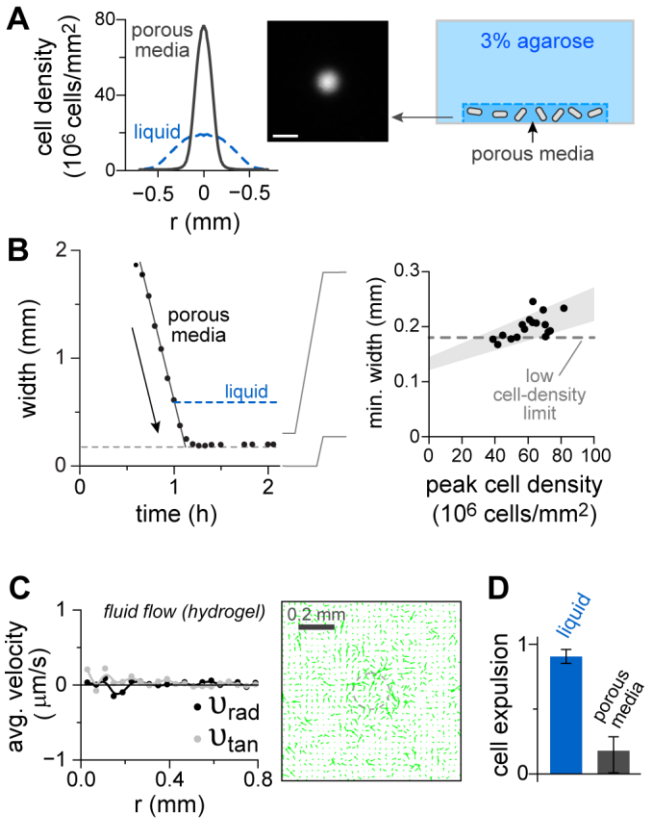

Figure 4. Bacterial condensation in porous media. Experiments similar to those described thus far were conducted, except that the cell suspension was mixed with low concentration of agarose (0.08% w/v), resulting in cells being embedded within a dilute hydrogel. General chemotactic behavior in this hydrogel medium is shown in Fig. S3. (**A**) Fluorescence image of a typical mature condensates condensate in porous medium (scale bar: 300 μm) along with the corresponding radially-averaged density profile. For comparison, a typical profile of a condensate observed in liquid is also shown (blue). A schematic description of the revised setup is also shown on the right. Because condensations in porous medium were significantly narrower, the diameter of the cell suspension was reduced to 3 mm to avoid the formation of multiple focal points (see ref. 14 and Materials and Methods). (**B**) The condensation dynamics in porous medium (left plot, black symbols). The saturation value of the condensate width in liquid is indicated by a dashed blue line, and the corresponding value at low cell-density (from ref. 18) is indicated by the gray dashed lines. *Inset* – The saturation width of the condensate in porous medium is plotted against the peak cell density for 17 experiments. Shaded gray region represents a linear fit to the data. (**C**) Fluid motion in porous medium. The 2D velocity field within the plane of the condensate was measured and analyzed as in Fig. 2. The time averaged velocity field (30 s) is shown (right) along with the radial and tangential velocity components plotted as a function of the distance from the center of the condensate (left). (**D**) Expulsion of non-chemotactic cells from the condensate was measured in porous media in experiments similar to those described in Fig. 3. Expulsion efficiency is defined as the ratio of the fluorescence intensity at the center of the condensation to that at the periphery.

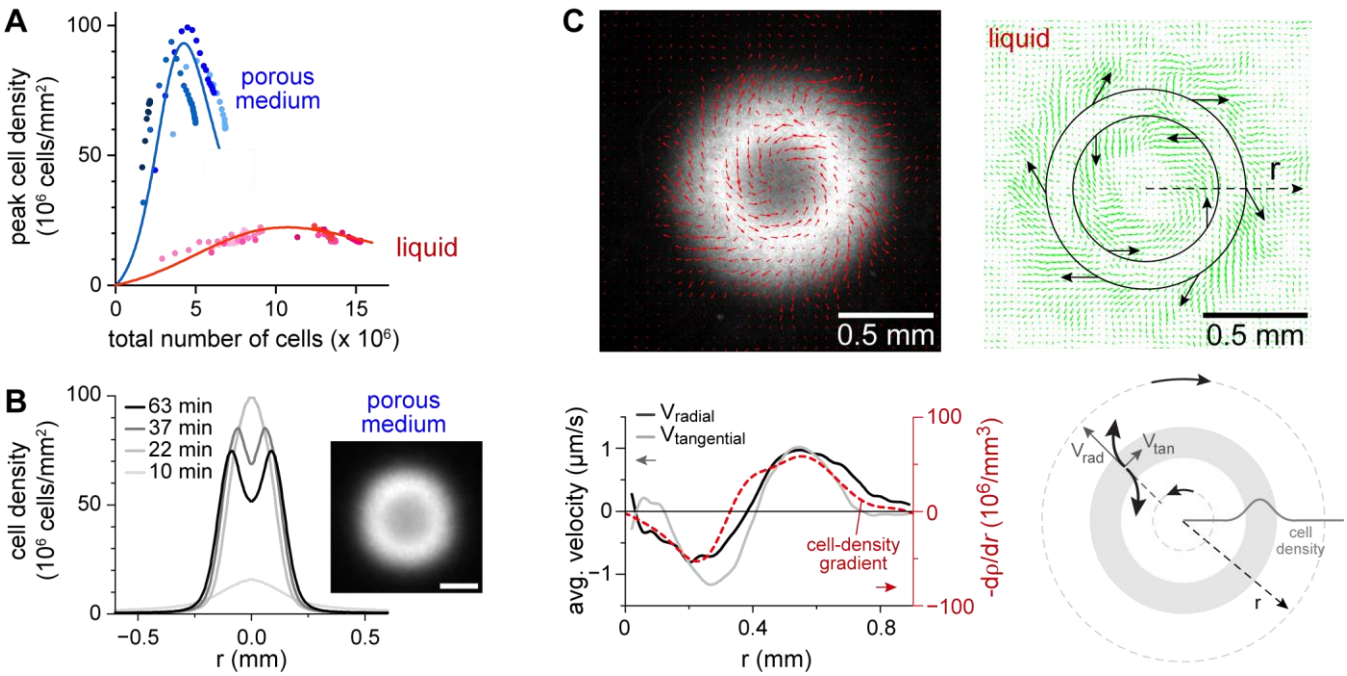

Figure 5. Condensation at even higher initial cell density. (**A**) The peak cell density is plotted against the total number of cells in the condensate for experiments performed with the cells in liquid (red symbols) or in porous medium (blue symbols). The total number of cells was modulated by the varying the initial (uniform) cell density. The decrease in the peak cell density observed at high cell numbers was correlated with the formation of ring-shaped condensation, demonstrated in (B) and (C). (**B**) *Porous medium*: A representative of a mature ring-shaped condensate. Evolution of the condensate profile is shown (left plot), along with a florescence image taken at 50 min (scale bar: 150 μm). (**C**) *Liquid medium*: A typical fluorescence image of a mature condensate at high cell number. Time-averaged bacterial velocity field, extracted using PIV, are overlaid on the image (red arrows), and also shown separately on the right (green arrows). Below the image, the radial and tangential velocity components are plotted as function of the distance from the condensate center, along with the corresponding cell-density gradient. A schematic shown on the right illustrates the correlated reversal of both velocity components across the ring, consistently producing a rightward swimming tendency in both the inner and outer regions.

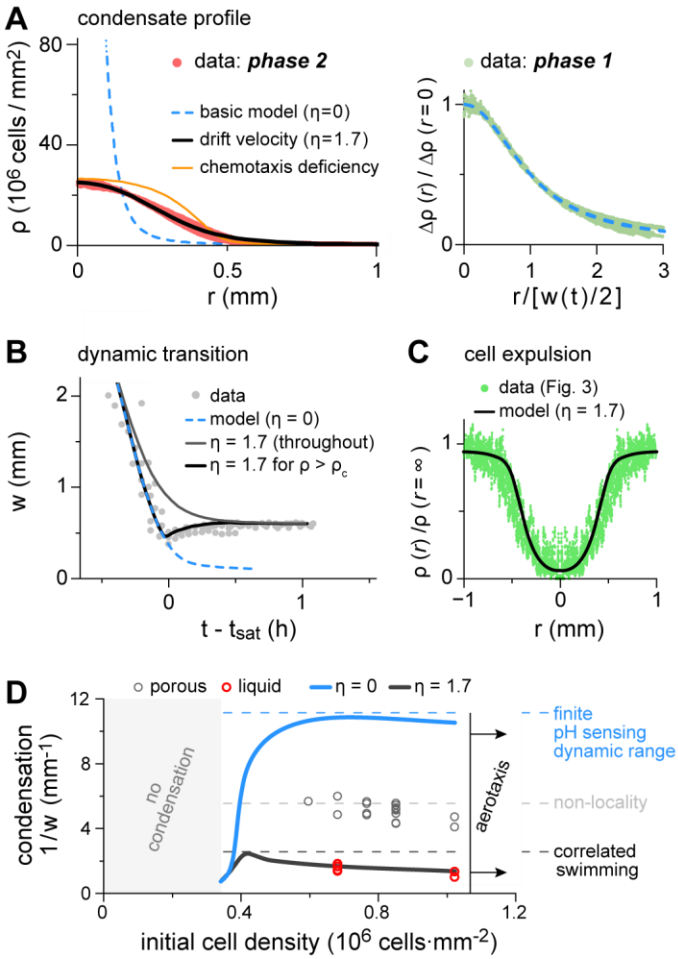

Figure 6. A model for condensate broadening by collective motion. Numerical solutions for the model described by Eqs. 1–3 were used to compare its predictions with the data obtained in liquid medium. Chemotaxis is described by Eqs. 1 and 2, and an additional outward velocity drift, $\vec{U} \sim -\eta \cdot \vec{\nabla}\rho$ (Eq. 3) is assumed be imposed by the active turbulence. The parameter η is given hereafter in units of 10^{-7} cm^2 s^{-1}. (**A**) *Condensation shape*. Measured condensate profiles from phase 1 (three independent experiments; see also Fig. 1) are well captured by the model with $\eta = 0$ (right plot; blue dashed line). However, a value of $\eta = 1.7$ was required to match the data from phase 2 (left plot, black line). We also tested a model with $\eta = 0$, but in which the chemotaxis efficiency (Eq. 1) depends on the local cell-density as described in ref. 30 (orange line; Fig. S8). (**B**) *Condensation dynamics*. The condensate width is plotted against time (gray symbols; 4 independent experiments, see Fig. 1). To capture the onset of active turbulence at a critical peak density ρ_c, we modeled allowed η to depend on the peak cell density ρ_c: $\eta \sim 1/(1+\exp(-(k/\rho_0)(\rho_{max}-\rho_c)))$, with ρ_0 being the initial (uniform) density, $k = 3$ and $\rho_c = 25 \cdot \rho_0$. (**C**) *Expulsion of non-chemotactic cells*. Data from Fig. 3 (green symbols) is replotted together with the corresponding distribution predicted by the model $\rho = \exp\{-(\eta/D_{NC}) \cdot (\rho_{WT}(r)/\rho_0)\}$ with η = 1.7, $\rho_{WT}(r)$ taken from the experimental data in (A), and $D_{NC} = 2.5 \cdot 10^{-6}$ cm^{2}s^{-1} representing the effective diffusion of the non-chemotactic cells (see derivation in Supp. text). (**D**) *Summary plot*. The saturated condensation level (defined as inverse width: 1/*w*) is plotted as a function of the initial (uniform) cell density. Data from experiments in liquid and porous media (empty circles) and the corresponding simulations (lines) are shown (as labeled). The vertical black line ('aerotaxis') indicates the density above which ring-shaped condensates appear. The low-density limit (18) is plotted as a dashed gray line ('non-locality'). The shaded gray region on the left ('no condensation') marks a range of concentrations that do not support condensation (14, 37).